Palaeoarchaean Deep Mantle Heterogeneity Recorded by 3.45 Ga Enriched Plume Remnants

Chao Wang[1,2]*, Shuguang Song[1]*, Chunjing Wei[1], Li Su[3], Mark B. Allen[4], Yaoling Niu[2,4], Xian-Hua Li[5], Jinlong Dong[1]

[1] *MOE Key Laboratory of Orogenic Belts and Crustal Evolution, School of Earth and Space Sciences, Peking University, Beijing 100871, China*

[2] *School of Earth Sciences and Resources, China University of Geosciences, Beijing 100083, China*

[3] *School of Scientific Research and State Key Laboratory of Geological Processes and Mineral Resources, China University of Geosciences, Beijing 100083, China*

[4] *Department of Earth Sciences, Durham University, Durham DH1 3LE, UK*

[5] *State Key Laboratory of Lithospheric Evolution, Institute of Geology and Geophysics, Chinese Academy of Sciences, Beijing 100029, China*

Revised manuscript for *Nature Geoscience*

*corresponding authors

Chao Wang (chao.wang@cugb.edu.cn)

Shuguang Song (sgsong@pku.edu.cn)

Cover note

Length of title: 84 characters including spaces.

Length of abstract: 175 words.

Length of main text: 2598 words.

Lenth of sub-headings: sub-heading #1, 34 characters including spaces; sub-heading #2, 42 characters including spaces; sub-heading #3, 57 characters including spaces.

Length of methods: 1491 words.

Length of legends: Figure 1, 79 words; Figure 2, 106 words; Figure 3, 120 words; Figure 4, 52 words; Figure 5, 134 words.

Number of references for main text (including legends): 42 references.

Number of references for methods: 18 references.

Number of references for Supplementary Information: 8 references.

Number and estimated final size of figures and tables: 5 Figures; Figures 1–3 need to be of two-column width; Figures 4–5 need to be of one-column width. 10 Supplementary Figures and 6 Suplementary Tables; all of them will be deposited in Supplementary Information files.

Abstract

The thermal and chemical state of the early Archaean deep mantle is poorly resolved due to rare occurrences of early Archaean highly magnesian volcanic rocks. Here we report the first discovery of a suite of Palaeoarchaean (3.45 Ga in situ zircon U-Pb age) ultramafic-mafic rocks with mantle plume signatures in Longwan, Eastern Hebei, the North China Craton. This suite consists of high-grade metamorphic lherzolite, pyroxenite, ferropicrite and ferrobasalt. The meta-ferropicrite and meta-ferrobasalt show geochemical characteristics of present-day oceanic island basalt and unusually high mantle potential temperatures (T_p = 1,675 °C), suggesting a deep mantle source enriched in iron and incompatible elements. The Longwan ultramafic-mafic suite is best interpreted as representing remnants of 3.45 Ga mantle plume magmatism. The first emergence of mantle plume-related rocks with various deep mantle sources on the Earth took place at 3.5–3.45 Ga, implying that a global mantle plume event occurred with the onset of large-scale deep mantle convection in the Palaeoarchaean, and significant compositional heterogeneity, most likely introduced by recycled crustal material, was present in the Palaeoarchaean deep mantle.

Highly magnesian lavas (e.g., komatiites and picrites) are rare in Earth history, and are typically produced by adiabatic decompression melting of upwelling mantle plumes that are significantly hotter than the ambient mantle[1–3]. Because of the close affinity of komatiites and picrites with their primary magmas, they can probe the thermal and chemical state of the Earth's thermal boundary layer from which mantle plumes originate through time[4–6]. Ultramafic rocks occur in the 3.8 Ga greenstone belts of the North Atlantic Craton, but accumulated evidence indicates that these rocks were not mantle plume-related[7–10]. Definite records of mantle plume activities began to emerge since ~3.5 Ga[1,2], including 3.5–3.46 Ga komatiites in the Onverwacht Group, Barberton, South Africa and Coonterunah, East Pilbara, Australia. Geochemistry of Archaean komatiites suggests that their deep mantle source was hot, and depleted or similar to primitive mantle, while geochemistry of post-Archaean komatiites indicates a colder and heterogeneous deep mantle reservoir with enriched components introduced by Earth's convection[4,5]. There are no records of enriched ultramafic rocks from the Palaeoarchaean (3.6–3.2 Ga), comparable to the picrites associated with Phanerozoic mantle plumes, but given the fragmentary nature of the geological record, it is not clear whether this reflects a genuine lack of deep mantle heterogeneity and deep mantle convection in the Palaeoarchaean, or a sampling bias.

Here we report for the first time a suite of Palaeoarchaean ultramafic-mafic rocks with a lithological assemblage of metamorphosed lherzolite, pyroxenite, ferropicrite and ferrobasalt in the North China Craton (NCC). Geochronological and geochemical evidence indicates that these ultramafic-mafic rocks are remnants of a 3.45 Ga

enriched mantle plume. Based on these findings, we propose that a global mantle plume event occurred in the Palaeoarchaean as a result of large-scale deep mantle convection, and significant compositional heterogeneity was present in the Palaeoarchaean deep mantle.

The Longwan ultramafic-mafic suite

The NCC is a rare craton in that it preserves ≥ 3.8 Ga crustal record, both from extant orthogneisses and from detrital zircons in younger metasedimentary rocks[11]. There was widespread Neoarchaean granulite-facies metamorphism and granitic magmatism as the result of micro-continental collision[12–14]. No Eoarchaean–Palaeoarchaean mantle-derived ultramafic-mafic rocks, especially mantle plume-related ultramafic-mafic rocks, have been reported before from the NCC. The studied ultramafic-mafic rocks were collected from the Longwan iron-mining area of Eastern Hebei in the Eastern Block of the NCC (Fig. 1a). The Longwan ultramafic-mafic suite, together with banded (or massive) iron quartzite and garnet-mica schist, occurs as hundreds-metre to kilometre-scaled tectonic slivers within Neoarchaean tonalite-trondhjemite-granodiorite (TTG) gneisses (Fig. 1b). The iron quartzite lenses have been mined, and the ultramafic-mafic rocks crop out as dark-coloured wall-rocks of the mining pits. Two major types of ultramafic-mafic rocks have been identified based on their mineral assemblages: (1) meta-cumulates and (2) meta-basalts. They were all metamorphosed and completely recrystallized under high-pressure (HP) granulite-facies metamorphism at the end of the Neoarchaean, and no primary igneous

98 textures remain. The meta-cumulates occur as lens-shaped blocks and are
99 meta-lherzolite and meta-websterite in composition (Supplementary Fig. 1a–c), and
100 strongly recrystallized samples developed an idioblastic texture with triple junction
101 grain boundaries close to 120° angles (Supplementary Fig. 2a–b). The meta-lherzolite
102 is a rare component in the meta-cumulates and has a mineral assemblage of olivine,
103 clinopyroxene, orthopyroxene, minor Al-rich spinel and opaque oxides
104 (Supplementary Fig. 2a). The meta-websterite consists of clinopyroxene,
105 orthopyroxene, amphibole, with accessory pyrite between them (Supplementary Fig.
106 2b). The meta-basalts are dark- to green-coloured massive outcrops (Supplementary
107 Fig. 1d–e) and mafic in composition. They were metamorphosed into two-pyroxene
108 granulites (clinopyroxene, orthopyroxene, plagioclase, quartz and opaque oxides) or
109 garnet-clinopyroxene granulites (garnet, clinopyroxene, plagioclase, quartz and
110 opaque oxides) (Supplementary Fig. 2c–d) with very weak or no foliation. All zircon
111 grains from meta-basalts are metamorphic without any magmatic cores, giving
112 metamorphic ages of ~2.5 Ga as a result of intensive Neoarchaean granulite-facies
113 tectonothermal events (our unpublished data).

114 One hundred and twenty-five zircon grains were extracted from a meta-websterite
115 sample J14-46c (~30 kg) of the Longwan ultramafic-mafic suite. Zircons are mostly
116 subhedral crystals, 50–100 μm in length and show clear core-rim textures; bright
117 cores with weakly oscillatory zoning are surrounded by dark rims in
118 cathodoluminescence (CL) images (Fig. 2a), indicative of metamorphic overgrowth
119 around magmatic cores[15]. There are apatite inclusions in the magmatic cores, but no

felsic mineral inclusions were identified within them (Supplementary Fig. 3). Twenty-eight magmatic cores and 17 metamorphic rims were analyzed, and U-Pb data are listed in Supplementary Table 1. Most analyses are discordant owing to lead loss and plot under the concordia curve (Fig. 2b). Twenty-eight magmatic cores yield a $^{207}Pb/^{206}Pb$ age range of 3,475 ± 14 to 3,302 ± 2 Ma (1σ) with Th/U ratios generally over 0.2. They lie along a discordant line that intersects the concordia at 3,456 ± 15 Ma with a mean square weighted deviation (MSWD) of 1.9 (Fig. 2b), which is in accordance with the concordia age (3,451 ± 3 Ma; MSWD = 0.36) and weighted mean $^{207}Pb/^{206}Pb$ age (3,454 ± 4 Ma; MSWD = 8.1) of 13 analyses indistinguishable from the concordia curve (Fig. 2c). Most of the concordant analyses have Th/U ratios above 1. Seventeen metamorphic rims give $^{207}Pb/^{206}Pb$ ages ranging between 3,279 ± 4 to 2,993 ± 22 Ma with Th/U ratios mostly below 0.1. They define a discordant line intercepting the concordia at 3,267 ± 20 Ma (MSWD = 3.9), with three concordant $^{207}Pb/^{206}Pb$ ages of 3,271 ± 1 to 3,238 ± 2 Ma. Nine concordant magmatic cores were chosen for in situ trace element analyses, and the data are listed in Supplementary Table 2. Their trace element ratios are typical of zircons from mantle-derived magma, and resemble zircons from plume-influenced settings (Supplementary Fig. 4). Thirteen concordant to near-concordant magmatic cores (discordance < 10%) from the meta-websterite sample J14-46c were selected for in situ Hf-O isotope analyses, and data are listed in Supplementary Table 3. These magmatic cores have initial $^{176}Hf/^{177}Hf$ ratios of 0.280569–0.280720 (calculated at the concordia age 3451 ± 3 Ma) with $\varepsilon_{Hf}(t)$ values of 0.2 to 5.6, and have mantle-like $\delta^{18}O$ values from 4.10‰ to 5.58‰

(Fig. 2d).

Bulk-rock major and trace element data of the studied samples are listed in Supplementary Table 4. Samples of the Longwan ultramafic-mafic suite have systematic compositional variation as shown in MgO-variation diagrams (Supplementary Fig. 5). The meta-lherzolite samples have low contents of SiO_2 (39.84–44.86 wt.%) and Al_2O_3 (3.80–5.44 wt.%), but high MgO (27.76–33.03 wt.%) and Mg# (84.1–85.3) (Fig. 3b). They are slightly enriched in light rare earth elements (LREEs) over heavy rare earth elements (HREEs) with $(La/Yb)_N$ ranging from 2.7 to 4.7 (Fig. 3d). These meta-lherzolites have high abundances of compatible elements such as Cr and Ni. The meta-websterites are characterized by high contents of SiO_2 (51.15–54.18 wt.%), MgO (23.28–26.55 wt.%) with accordingly high Mg# (85.5–86.8) (Fig. 3b), and compatible elements (e.g., Cr and Ni). They are relatively low in TiO_2 (0.13–0.16 wt.%), Al_2O_3 (3.56–4.08 wt.%) and Fe_2O_{3T} (8.30–8.91 wt.%). They have similar trace element patterns compared with the meta-lherzolite samples (Fig. 3d). They show relative depletion of high field strength elements (HFSEs; e.g., Nb, Ta, Zr and Hf) (Fig. 3d). All the meta-basalts are iron-rich with Fe_2O_{3T} mostly > 14 wt.% and variable MgO contents (7.29–19.36 wt.%), and plot in the 'Alkali basalt' field (Fig. 3a). According to their MgO contents, they can be further subdivided into meta-ferropicrites (MgO > 12 wt.%) and meta-ferrobasalts (MgO < 12 wt.%). The meta-ferropicrites have high contents of TiO_2 (1.61–2.10 wt.%), MgO (12.57–19.36 wt.%), Cr (1,162–1,494 ppm) and Ni (411–943 ppm) with SiO_2 of 43.73–49.78 wt.% and Mg# of 62.1–71.9 (Fig. 3b). They are relatively enriched in Fe_2O_{3T} (15.24–16.89

wt.%) (Fig. 3c) but low in Al_2O_3 (4.65–7.85 wt.%). Their REE abundances are much higher than those of meta-cumulates, and they also show enrichment of LREEs over HREEs ($(La/Yb)_N$ = 6.7–8.6), ranging between the enriched mid-ocean ridge basalt (E-MORB) and the ocean island basalt (OIB) but having a closer affinity with OIB. They are depleted in Y and some HFSEs (e.g., Zr and Hf), but have positive anomalies of Nb and Ta (Fig. 3d). The meta-ferrobasalts have similar geochemical features to the meta-ferropicrites, except that they have lower MgO (7.29–9.36 wt.%) and Fe_2O_{3T} (11.19–15.68 wt.%) with Mg# of 50.6–62.0 and relatively high Al_2O_3 (6.80–11.05 wt.%) and CaO (14.36–18.05 wt.%). They also have relatively high abundances of Cr (825–1,394 ppm) and Ni (499–839 ppm).

Remnants of Palaeoarchaean plume magmatism

The absence of felsic mineral inclusions (Supplementary Fig. 3), and the sharp contrast of age population, Th/U ratios and $\varepsilon_{Hf}(t)$ values between magmatic zircon cores from the meta-websterite sample J14-46c and pre-2.8 Ga detrital or xenocrystic zircons from Eastern Hebei (Supplementary Figs. 6 and 7) argue against a xenocrystic origin of these zircons. Instead, morphological characteristics in CL images, high Th/U ratios, trace element systematics with close plume affinity and mantle-like Hf-O isotopic compositions demonstrate that these zircon cores were crystallized from mantle-derived magma at ~3.45 Ga (Fig. 2 and Supplementary Fig. 4). Even though the Longwan ultramafic-mafic rocks experienced HP granulite-facies metamorphism at the end of the Neoarchaean, most of their trace elements (e.g., REEs and HFSEs)

were relatively immobile during the Neoarchaean orogenic events, because these elements have positive linear correlations with Zr (Supplementary Fig. 8). The high Cr and Ni concentrations of meta-basalts argue that their elevated MgO contents are of original magmatic significance without metamorphic modification.

The meta-websterites are unlike any ultramafic-mafic lavas (e.g., komatiites, picrites and boninites), but similar to experimental and natural pyroxenite cumulates[16,17] (Fig. 3b), suggesting that they were crystallized from MgO-rich melts. The meta-lherzolites are also of cumulate origin, evidenced by their identical trace element patterns to meta-websterites (Fig. 3d). The correlation of Ni and V against Cr of the meta-basalts (Supplementary Fig. 9) implies that their protolith magmas experienced clinopyroxene-dominated (with olivine) fractionation. In addition, the meta-cumulates and the meta-basalts show complementary trends on Harker diagrams (Supplementary Fig. 5) and have almost indistinguishable ratios of Nb/Ta, Zr/Hf and Tb/Dy (Supplementary Fig. 10). Thus, it is highly likely that meta-cumulates were crystallized from the same magmas parental to the meta-basalts when ascending and cooling to shallower magma chambers. Using bulk-rock Mg# of the meta-cumulates and Fe-Mg exchange coefficients, we calculate Mg# and liquidus temperatures of the melts crystallizing cumulus minerals (see Methods). The results show that protoliths of the meta-cumulates were crystallized from relatively evolved melts with Mg# of 62.2–67.8 at temperature of ca. 1200 °C (Supplementary Table 5). As for their crystallizing pressures, the lack of garnet in the meta-cumulates and their low Al_2O_3 contents point to a shallow depth at least below the garnet stability field, i.e.,

spinel/plagioclase stability fields (~1–2 GPa).

The elevated iron contents of the meta-ferropicrites are distinguishable from typical picrites/komatiites but similar to iron-rich ferropicrites/ferrokomatiites (Fig. 3c). The meta-ferrobasalts (MgO < 12 wt.%) have similar elevated iron contents and trace element characteristics with the meta-ferropicrites (Fig. 3). The meta-basalts are all enriched in compatible elements (Cr, Co and Ni), suggesting a derivation from relatively high-degree melting of the mantle source. They are also enriched in Nb, Ta, Ti and LREEs, and their trace element patterns are similar to those of present-day OIB, indicative of an enriched mantle source (Fig. 3d). The uniformly high $(Gd/Yb)_N$, low Al_2O_3/TiO_2 ratios and Zr-Hf depletion indicate the presence of residual garnet in their mantle source as garnet prefers to hold Zr, Hf, HREEs and Al_2O_3 at high pressures (Figs. 3d and 4a). Their MgO-CaO systematics show that they were primarily derived from peridotite source with minor contribution from pyroxenite[18] (Fig. 4b). Therefore, the meta-ferropicrites have close affinity with primary magmas, while the meta-ferrobasalts with lower MgO and Mg# could represent evolved melts from those of the meta-ferropicrites after fraction of clinopyroxene and olivine (Supplementary Fig. 9).

Using FractionatePT software[19], we calculate melting conditions for primary magmas of the most primitive meta-ferropicrite samples (Supplementary Table 6) and results indicate that their primary magmas were derived from melting of mantle lherzolite at high pressures/temperatures (P = 5.7–6.7 GPa, T = 1,756–1,776 °C) (Fig. 5), corresponding to a mantle potential temperature (T_p) of 1,725 °C. However,

experimental studies have demonstrated that iron-rich lherzolites have systematicly lower solidus temperatures than fertile peridotites by ~50 °C[20], and thus the T_p for the meta-ferropicrites should be conservatively corrected to be 1,675 °C. The melting conditions and T_p are comparable to those for Palaeoarchaean komatiites in Barberton and East Pilbara (Fig. 5). The above lines of evidence clearly point to a derivation of primary magmas of the meta-basalts through melting of an anomalously hot mantle source at high pressures.

It is well accepted that the thermal regime in the Archaean was hotter than the present[21]. However, the estimated T_p for the Longwan meta-ferropicrites is 1,675 °C, implying that their mantle source was considerably hotter than the ambient mantle with T_p of 1,500–1,600 °C at 3.45 Ga[5]. Such conditions, when ascending mantle material is significantly hotter than the surrounding mantle, are consistent with the mantle plume model[22,23]. Besides, the high Ni contents of the Longwan meta-basalts argue for a strong affinity to mantle plume-related rocks than their lower-temperature counterparts[4]. Ferropicrites are rare throughout the geological history, and most Phanerozoic ferropicrite examples were identified at or near the base of volcanic sequences in continental large igneous province (LIP) or continental flood basalt province settings, with a few cases in accreted oceanic plateaus[24,25]. It is generally acknowledged that LIPs result from the arrival of a mantle plume head at the base of the lithosphere[26–28]. Thus, it is most likely that the Longwan ultramafic-mafic suite represents remnants of dismembered volcanic successions generated during a Palaeoarchaean (~3.45 Ga) mantle plume activity.

Implications for Palaeoarchaean deep mantle heterogeneity

Mantle plume activities were infrequent through the Archaean compared with the Proterozoic and the Phanerozoic[29]. Komatiites and komatiitic basalts were generated by adiabatic decompression melting of upwelling mantle plumes at high mantle potential temperatures and pressures, and serve as records of mantle plume activities[2,5]. The 3.45 Ga Longwan ultramafic-mafic suite reported in this study, and the 3.5–3.46 Ga komatiites preserved in Barberton and East Pilbara, are the oldest confirmed records of mantle plume activities[1,2]. These Palaeoarchaean mantle plume-related rocks could be a record of the oldest global mantle plume event in the Earth's history and a counterpart to younger occurrences of global mantle plume activities[30]. This global mantle plume event may indicate that large-scale deep mantle convection has been operating since the Palaeoarchaean.

Partial melting of a typical peridotitic mantle alone cannot explain the iron-rich features observed in ferropicrites[24,31–33]. It is commonly suggested that Archaean ferropicrites required an iron-rich peridotitic mantle source, though how to reach this iron enrichment remains controversial: addition of recycled crustal material, an initially iron-rich mantle and subsequent iron sequestration, a core contribution and even an infall of iron-rich chondritic meteorites[24,31–37]. Nonetheless, the occurrence of meta-ferropicrites and meta-ferrobasalts in the ~3.45 Ga Longwan ultramafic-mafic suite indicates the existence of iron-rich domains in their Palaeoarchaean deep mantle source. In addition, the enriched REE patterns and the relatively high melting degrees

of these meta-ferropicrites and meta-ferrobasalts require an enriched deep mantle source, whereas the depleted and flat REE patterns of the 3.5–3.46 Ga komatiites in Barberton and East Pilbara imply a depleted or primitive deep mantle source[1,2,4] (Fig. 3d). Therefore, deep mantle heterogeneity was present in the Palaeoarchaean, with partial enrichment of iron and incompatible elements. Enriched domains in the Palaeoarchaean deep mantle are most probably caused by the incorporation of recycled crustal material[24,25,31], and indicate interaction between lithosphere and mantle plumes, and crustal recycling processes.

Figure legends

Figure 1 Geological maps of Eastern Hebei, the NCC and the study area. a, Inset is a sketch map of the NCC showing its major tectonic units. Eastern Hebei lies in the Eastern Block of the NCC and its Precambrian basement rocks consist of Neoarchaean TTG gneisses, charnockites, and supracrustal rocks with some Palaeo-Mesoarchaean supracrustal remnants and Palaeoproterozoic mafic dykes. **b**, The studied meta-cumulate and meta-basalt samples were collected from meta-supracrsutal lenses from the Longwan iron-mining area of Eastern Hebei, which are within the Neoarchaean TTG gneisses and intruded by Mesozoic plutons.

Figure 2 CL images, U-Pb concordia diagrams and Hf-O isotopes for zircons from the meta-websterite sample J14-46c the Palaeoarchaean Longwan ultramafic-mafic suite. a, CL images of representative zircons from the

meta-websterite sample J14-46c; ellipses are in situ SIMS zircon U-Pb analytical spots; numbers in ellipses are sequential numbers of analytical spots; ages next to ellipses are zircon $^{207}Pb/^{206}Pb$ ages; scale bars are 20 μm in length. **b**, U-Pb concordia diagram for all zircons from the meta-websterite sample J14-46c. **c**, U-Pb concordia diagram for concordant magmatic zircon cores from the meta-websterite sample J14-46c; inset is the weighted mean $^{207}Pb/^{206}Pb$ age of concordant magmatic zircon cores. **d**, $\varepsilon_{Hf}(t)$-$\delta^{18}O$ diagram for magmatic zircon cores with discordance < 10% from the meta-websterite sample J14-46c; mantle zircon $\delta^{18}O$ values are from ref. 38.

Figure 3 Geochemical diagrams for the Palaeoarchaean Longwan ultramafic-mafic suite. **a**, Rock classification diagram[39] for meta-basalts with meta-cumulates plotted for comparison. **b**, SiO_2-MgO diagram; fields of komatiites, picrites, basalts and bonnites are constructed using the data from the GEOROC database with experimentally-produced pyroxenite cumulates[16] plotted for comparison. **c**, SiO_2-FeOt diagram; fields of ferropicrite/ferrokomatiite, picrite/komatiite and Iceland/MORB are form ref. 24. Major element oxides in **a**, **b** and **c** are recalculated on an anhydrous basis. **d**, Primitive mantle-normalized trace element diagram; values of primitive mantle, OIB and E-MORB are from ref. 40 and values of 3.5–3.46 Ga komatiites in Barberton and East Pilbara are from ref. 3; only fluid immobile elements are plotted because they should not have been affected during high-grade metamorphism and can be used for petrogenetic interpretations.

Figure 4 Geochemical diagrams for the meta-basalts of the Palaeoarchaean Longwan ultramafic-mafic suite. a, Al_2O_3/TiO_2-$(Gd/Yb)_N$ diagram after ref. 41; N denotes chondrite-normalized; chondrite and OIB values are from ref. 40. **b**, MgO-CaO diagram after ref. 18; the dashed line is the boundary to differentiate between peridotite-sourced melts (above the line) and pyroxenite-sourced melts (below the line). Major element oxides are recalculated on an anhydrous basis.

Figure 5 Calculated melting conditions for primary magmas of the meta-ferropicrites of the Palaeoarchaean Longwan ultramafic-mafic suite. Melting conditions for primary magmas of the most primitive meta-ferropicrite samples with the highest MgO contents (15LW-13 and 17LW-08) are calculated using thermobarometers based on magma Si and Mg contents[19]. Potential temperatures (T_p) are estimated by back-calculating melting conditions of primary magmas along an isentropic melting adiabat until the melting adiabat intersects the solidus and then extrapolating from this intersection point along a solid mantle adiabat to the surface. Dry lherzolite solidus and liquidus are from ref. 42; Fe-rich lherzolite solidus (heavy dashed line) is estimated via lowering the dry lherzolite solidus by ~50 °C[20]; blue near-vertical lines represent solid mantle adiabats with varying mantle potential temperatures (T_p); the red curved line with arrow corresponds to the isentropic melting adiabat; melting conditions for MORB, Hawaii Hotspot basalt and Palaeoarchaean komatiite are from ref. 19.

Online content

Methods, including statements of data availability and associated references, and Supplementary Information files are available in the online version of this paper.

References

1. Arndt NT, Lesher CM, Barnes SJ. *Komatiite*. Cambridge University Press, 2008.
2. Barnes SJ, Arndt NT. Chapter 6 - Distribution and geochemistry of komatiites and basalts through the Archean. In: Van Kranendonk MJ, Bennett VC, Hoffmann JE (eds). *Earth's Oldest Rocks (Second Edition)*. Elsevier, 2019, pp 103-132.
3. Sossi PA, Eggins SM, Nesbitt RW, Nebel O, Hergt JM, Campbell IH*, et al.* Petrogenesis and Geochemistry of Archean Komatiites. *Journal of Petrology* 2016, **57**(1)**:** 147-184.
4. Campbell I, Griffiths R. The changing nature of mantle hotspots through time: implications for the chemical evolution of the mantle. *The Journal of Geology* 1992, **100**(5)**:** 497-523.
5. Herzberg C, Condie K, Korenaga J. Thermal history of the Earth and its petrological expression. *Earth and Planetary Science Letters* 2010, **292**(1-2)**:** 79-88.
6. Nisbet EG, Cheadle MJ, Arndt NT, Bickle MJ. Constraining the potential temperature of the Archaean mantle: A review of the evidence from komatiites. *Lithos* 1993, **30**(3)**:** 291-307.
7. Dymek RF, Brothers SC, Schiffries CM. Petrogenesis of Ultramafic Metamorphic

Rocks from the 3800 Ma Isua Supracrustal Belt, West Greenland. *Journal of Petrology* 1988, **29**(6)**:** 1353-1397.

8. Collerson KD, Campbell LM, Weaver BL, Palacz ZA. Evidence for extreme mantle fractionation in early Archaean ultramafic rocks from northern Labrador. *Nature* 1991, **349:** 209-214.

9. Polat A, Hofmann AW, Rosing MT. Boninite-like volcanic rocks in the 3.7–3.8 Ga Isua greenstone belt, West Greenland: geochemical evidence for intra-oceanic subduction zone processes in the early Earth. *Chemical Geology* 2002, **184**(3–4)**:** 231-254.

10. O'Neil J, Francis D, Carlson RW. Implications of the Nuvvuagittuq Greenstone Belt for the Formation of Earth's Early Crust. *Journal of Petrology* 2011, **52**(5)**:** 985-1009.

11. Liu DY, Nutman AP, Compston W, Wu JS, Shen QH. Remnants of ≥3800 Ma crust in the Chinese part of the Sino-Korean craton. *Geology* 1992, **20**(4)**:** 339-342.

12. Nutman AP, Wan Y, Du L, Friend CRL, Dong C, Xie H*, et al.* Multistage late Neoarchaean crustal evolution of the North China Craton, eastern Hebei. *Precambrian Research* 2011, **189**(1–2)**:** 43-65.

13. Zhai M-G, Santosh M, Zhang L. Precambrian geology and tectonic evolution of the North China Craton. *Gondwana Research* 2011, **20**(1)**:** 1-5.

14. Wang C, Song S, Niu Y, Wei C, Su L. TTG and Potassic Granitoids in the Eastern North China Craton: Making Neoarchean Upper Continental Crust during

Micro-continental Collision and Post-collisional Extension. *Journal of Petrology* 2016, **57**(9)**:** 1775-1810.

15. Corfu F, Hanchar JM, Hoskin PW, Kinny P. Atlas of zircon textures. *Reviews in Mineralogy and Geochemistry* 2003, **53**(1)**:** 469-500.

16. Müntener O, Kelemen PB, Grove TL. The role of H2O during crystallization of primitive arc magmas under uppermost mantle conditions and genesis of igneous pyroxenites: an experimental study. *Contributions to Mineralogy and Petrology* 2001, **141**(6)**:** 643-658.

17. Lee C-TA, Cheng X, Horodyskyj U. The development and refinement of continental arcs by primary basaltic magmatism, garnet pyroxenite accumulation, basaltic recharge and delamination: insights from the Sierra Nevada, California. *Contributions to Mineralogy and Petrology* 2006, **151**(2)**:** 222-242.

18. Herzberg C, Asimow PD. Petrology of some oceanic island basalts: PRIMELT2.XLS software for primary magma calculation. *Geochemistry, Geophysics, Geosystems* 2008, **9**(9)**:** Q09001.

19. Lee C-TA, Luffi P, Plank T, Dalton H, Leeman WP. Constraints on the depths and temperatures of basaltic magma generation on Earth and other terrestrial planets using new thermobarometers for mafic magmas. *Earth and Planetary Science Letters* 2009, **279**(1-2)**:** 20-33.

20. Kushiro I. Partial Melting of a Fertile Mantle Peridotite at High Pressures: An Experimental Study Using Aggregates of Diamond. *Earth Processes: Reading the Isotopic Code*, vol. 95, 1996, pp 109-122.

21. Richter FM. Models for the Archean thermal regime. *Earth and Planetary Science Letters* 1985, **73**(2-4)**:** 350-360.

22. Campbell IH, Griffiths RW, Hill RI. Melting in an Archaean mantle plume: heads it's basalts, tails it's komatiites. *Nature* 1989, **339:** 697-699.

23. Campbell IH, Griffiths RW. Implications of mantle plume structure for the evolution of flood basalts. *Earth and Planetary Science Letters* 1990, **99**(1)**:** 79-93.

24. Gibson SA. Major element heterogeneity in Archean to Recent mantle plume starting-heads. *Earth and Planetary Science Letters* 2002, **195**(1)**:** 59-74.

25. Jennings ES, Holland TJB, Shorttle O, Maclennan J, Gibson SA. The Composition of Melts from a Heterogeneous Mantle and the Origin of Ferropicrite: Application of a Thermodynamic Model. *Journal of Petrology* 2016, **57**(11-12)**:** 2289-2310.

26. Coffin MF, Eldholm O. Large igneous provinces: Crustal structure, dimensions, and external consequences. *Reviews of Geophysics* 1994, **32**(1)**:** 1-36.

27. Saunders AD. Large igneous provinces: origin and environmental consequences. *Elements* 2005, **1**(5)**:** 259-263.

28. Ernst RE, Jowitt SM. Large igneous provinces (LIPs) and metallogeny. *Tectonics, Metallogeny, and Discovery: the North American Cordillera and Similar Accretionary Settings Edited by M Colpron, T Bissig, BG Rusk, and JFH Thompson Society of Economic Geologists Special Publication* 2013, **17:** 17-51.

29. Ernst R, Bleeker W. Large igneous provinces (LIPs), giant dyke swarms, and

mantle plumes: significance for breakup events within Canada and adjacent regions from 2.5 Ga to the Present. *Canadian Journal of Earth Sciences* 2010, **47**(5)**:** 695-739.

30. Barley ME, Krapez B, Groves DI, Kerrich R. The Late Archaean bonanza: metallogenic and environmental consequences of the interaction between mantle plumes, lithospheric tectonics and global cyclicity. *Precambrian Research* 1998, **91**(1)**:** 65-90.

31. Gibson SA, Thompson RN, Dickin AP. Ferropicrites: geochemical evidence for Fe-rich streaks in upwelling mantle plumes. *Earth and Planetary Science Letters* 2000, **174**(3)**:** 355-374.

32. Milidragovic D, Francis D. Ca. 2.7Ga ferropicritic magmatism: A record of Fe-rich heterogeneities during Neoarchean global mantle melting. *Geochimica et Cosmochimica Acta* 2016, **185:** 44-63.

33. Zhang J, Liu Y, Ling W, Gao S. Pressure-dependent compatibility of iron in garnet: Insights into the origin of ferropicritic melt. *Geochimica et Cosmochimica Acta* 2017, **197:** 356-377.

34. Hanski EJ, Smolkin VF. Iron- and LREE-enriched mantle source for early Proterozoic intraplate magmatism as exemplified by the Pechenga ferropicrites, Kola Peninsula, Russia. *Lithos* 1995, **34**(1)**:** 107-125.

35. Stone WE, Crocket JH, Dickin AP, Fleet ME. Origin of Archean ferropicrites: geochemical constraints from the Boston Creek Flow, Abitibi greenstone belt, Ontario, Canada. *Chemical Geology* 1995, **121**(1)**:** 51-71.

446 36. Francis D, Ludden J, Johnstone R, Davis W. Picrite evidence for more Fe in
447 Archean mantle reservoirs. *Earth and Planetary Science Letters* 1999, **167**(3)**:**
448 197-213.
449 37. Goldstein SB, Francis D. The Petrogenesis and Mantle Source of Archaean
450 Ferropicrites from the Western Superior Province, Ontario, Canada *Journal of*
451 *Petrology* 2008, **49**(10)**:** 1729-1753.
452 38. Valley JW. Oxygen isotopes in zircon. *Reviews in Mineralogy and Geochemistry*
453 2003, **53**(1)**:** 343-385.
454 39. Winchester JA, Floyd PA. Geochemical discrimination of different magma series
455 and their differentiation products using immobile elements. *Chemical Geology*
456 1977, **20:** 325-343.
457 40. Sun SS, McDonough WF. Chemical and isotopic systematics of oceanic basalts:
458 implications for mantle composition and processes. *Geological Society, London,*
459 *Special Publications* 1989, **42**(1)**:** 313-345.
460 41. Arndt N. Komatiites, kimberlites, and boninites. *Journal of Geophysical Research:*
461 *Solid Earth* 2003, **108**(B6)**:** 2002JB002157.
462 42. Katz RF, Spiegelman M, Langmuir CH. A new parameterization of hydrous
463 mantle melting. *Geochemistry, Geophysics, Geosystems* 2003, **4**(9)**:**
464 2002GC000433.

465 Acknowledgements

466 We thank S. Gibson for constructive discussions. This study was supported by the

National Natural Science Foundation of China (grant No. 41430207, 41372060, 41572040) and the Fundamental Research Funds for the Central Universities of China (grant No. 2652018115). C.W. acknowledges Chinese Scholarship Council for the financial support during his visit to Durham University (grant No. 201606010063).

Author contributions

C.W. and S.S designed the project and wrote the manuscript. C.W., S.S., C.J.W. and J.D. conducted fieldwork. C.W., L.S. and X.-H.L performed all the analyses. All authors contributed to the interpretation of the results and the revision of the manuscript.

Competing interests

The authors declare no competing interests.

Additional information

Supplementary information is available in the online version of the paper.

Correspondence and requests for materials should be addressed to C.W. and S.S.

Methods

In situ zircon U-Pb dating. Zircon grains were extracted from crushed samples by standard heavy-liquid and magnetic techniques, and purified by hand-picking under a binocular microscope. The selected grains were mounted in epoxy resin and polished

485 down to about half-sections to expose the grain interiors, and then imaged under
486 reflected and transmitted lights and by using CL. The CL images were acquired using
487 a Panchromatic CL detector installed on a MIRA3 scanning electron microscope at
488 MOE Key Laboratory of Orogenic Belts and Crustal Evolution, School of Earth and
489 Space Sciences, Peking University, Beijing. Mineral inclusions in zircons were
490 identified using an Oxford INCA-Synergy energy dispersive spectroscopy installed on
491 a FEI FEG 650 scanning electron microscope (SEM-EDS) at Peking University.

492 Measurements of zircon U, Th and Pb isotopes were conducted using the
493 CAMECA IMS-1280 secondary ion mass spectrometry (SIMS) at the Institute of
494 Geology and Geophysics, Chinese Academy of Sciences (IGGCAS) in Beijing,
495 following the standard procedures described in ref. 43. The primary O^{2-} ion beam spot
496 is about 20×30 μm in size. Analyses of the standard zircon Plešovice were
497 interspersed with unknown grains. Pb/U calibration was performed relative to zircon
498 standard Plešovice[44]; U and Th concentrations were calibrated against zircon standard
499 91500[45]. In order to monitor the external uncertainties of SIMS U-Pb zircon dating
500 calibrated against Plešovice standard, an in-house zircon standard Qinghu was
501 alternately analyzed as an unknown together with other unknown zircons. Fifteen
502 measurements on Qinghu zircon yield a concordia age of 159.9 ± 1.2 Ma, which is
503 identical within error with the recommended value of 159.5 ± 0.2 Ma[46]. A long-term
504 uncertainty of 1.5% (1 relative standard deviation) for $^{206}Pb/^{238}U$ measurements of the
505 standard zircons was propagated to the unknowns. Measured compositions were
506 corrected for common Pb using non-radiogenic ^{204}Pb. Corrections are sufficiently

small to be insensitive to the choice of common Pb composition, and an average of present-day crustal composition[47] is used for the common Pb assuming that the common Pb is largely surface contamination introduced during sample preparation. Data reduction was carried out using the Isoplot/Ex ver. 3.0[48]. Uncertainties of individual analyses in data tables are reported at 1σ level.

In situ zircon oxygen isotope analyses. After U-Pb dating, the sample mount was re-ground and re-polished to ensure that any oxygen implanted in the zircon surface from the O^{2-} beam used for U-Pb dating was removed. Zircon oxygen isotopes were measured using the CAMECA IMS-1280 SIMS at IGGCAS, following standard procedures described in ref. 49. The primary Cs^{+} ion beam spot was 10 μm in size. Oxygen isotopes were measured using multi-collection mode on two off-axis Faraday cups. The instrumental mass fractionation factor (IMF) was corrected using the zircon standard 91500 with a $\delta^{18}O$ value of 9.9‰[50]. Measured $^{18}O/^{16}O$ ratios were normalized using the Vienna Standard Mean Ocean Water compositions (VSMOW: $^{18}O/^{16}O = 0.0020052$), and then reported in standard per mil notation. A second zircon standard Qinghu was also analyzed as an unknown to ascertain the veracity of the IMF. Uncertainties on individual analyses are reported at 1σ level. The internal precision of a single analysis is generally better than 0.2‰ (2σ) for $^{18}O/^{16}O$ ratio. The external reproducibility of $^{18}O/^{16}O$ ratios by repeated measurements of standard zircon is better than 0.40‰. Twenty-four measurements of Qinghu zircon standard during the course of this study yielded a weighted mean of $\delta^{18}O = 5.38 \pm 0.12$‰ (2σ, n = 24), which is consistent within errors with the reported value of 5.4 ± 0.2‰[46].

In situ zircon Hf isotope analyses. In situ zircon Hf isotope analyses of the dated sample were carried out using a Neptune multi-collector inductively coupled plasma mass spectrometry attached with a New Wave UP-213 laser-ablation system (LA-MC-ICPMS) at MLR Key Laboratory of Metallogeny and Mineral Assessment, Institute of Mineral Resources, Chinese Academy of Geological Sciences, Beijing. Analytical details are given in ref. 51. Laser spot size of 40 μm was adopted for analyses and Helium gas was used as carrier gas to transport the laser ablated sample from the laser-ablation cell to the ICPMS torch via a mixing chamber mixed with Argon gas. Correction for the isobaric interferences of ^{176}Lu and ^{176}Yb on ^{176}Hf was after ref. 51. Before the analyses, standard zircons (TEMORA, GJ1 and FM02) were analyzed and the efficacy of the correction method of isobaric interferences in ref. 51 was tested to be efficient. Zircon GJ1 was used as the reference standard to monitor data quality during analyses, giving a weighted mean ^{176}Hf/^{177}Hf ratio of 0.282015 ± 9 (2σ, n = 9), which is in accordance with the weighted mean ^{176}Hf/^{177}Hf ratio of 0.282000 ± 5 (2σ) measured by the solution analysis method[52].

In situ zircon trace element analyses. Measurement of trace elements in zircons were carried out on an Agilent-7500a quadrupole inductively coupled plasma mass spectrometer coupled with a New Wave UP-193 solid-state laser-ablation system (LA-ICPMS) in the Geological Lab Center, China University of Geosciences, Beijing (CUGB). A laser spot size of 36 μm, laser energy density of 8.5 J cm^{-2} and a repetition rate of 10 Hz were used for analyses. The ablated sample material was carried into the ICPMS system by high-purity helium gas. Calibrations for element

concentration were carried out using NIST 610 glass and Harvard standard zircon 91500 as external standards, with recommended values taken from refs. 45 and 53 and using ^{29}Si as an internal standard. NIST 612 and 614 glasses served as monitoring standards at the same time. The analytical accuracy for trace elements in zircon is better than ±10% with abundances > 10 ppm, and ±15% with abundances < 10 ppm.

Bulk-rock major and trace element analyses. All the samples are fresh cuttings away from late veinlets, with any surface contaminants trimmed off before being thoroughly cleaned. Fresh portions of the trimmed samples were crushed into 1–2 cm size chips using a percussion mill. These rock fragments were ultrasonically cleaned in Milli-Q water, dried and powdered in a thoroughly cleaned agate mill to 200 mesh in the clean laboratory at the Langfang Regional Geological Survey, China. Bulk-rock major and trace element analyses were done in the Geological Lab Center, CUGB following the procedures described in ref. 54. Major elements were analyzed on a Leeman Prodigy inductively coupled plasma-optical emission spectroscopy (ICP-OES) system with high dispersion Echelle optics. Based on rock standards AGV-2, W-2 (US Geological Survey: USGS), GSR-1 and GSR-3 (national geological standard reference material of China), the analytical precisions (1σ) for most major element oxides are better than 1% with the exception of TiO_2 (~1.5%) and P_2O_5 (~2.0%). Loss on ignition (LOI) was determined by placing 1 g of samples in the furnace at 1000 °C for a few hours and then reweighting the cooled samples.

Bulk-rock trace elements were analyzed using an Agilent-7500a quadrupole inductively coupled plasma mass spectrometry (ICPMS). About 35 mg powder of

each sample was dissolved in distilled acid mixture (1:1 HF + HNO_3) with Teflon digesting vessels and heated on a hot-plate at 195 °C for 48 hours using high-pressure bombs for digestion/dissolution. The sample was then evaporated to incipient dryness, refluxed with 1 mL of 6 N HNO_3 and heated again to incipient dryness. The sample was again dissolved in 2 mL of 3 N HNO_3 and heated at 165 °C for further 24 hours to guarantee complete digestion/dissolution. The sample was finally diluted with Milli-Q water to a dilution factor of 2,000 in 2% HNO_3 solution for ICPMS analyses. Rock standards AGV-2, W-2 and BHVO-2 (USGS) were used to monitor the analytical accuracy and precision. Analytical accuracy, as indicated by relative difference between measured and recommended values is better than 5% for most elements, and 10 ~ 15% for Cu, Zn, Gd, and Ta.

Calculation of Mg# and liquidus temperatures for melts in equilibrium with meta-cumulates. Cumulus minerals should be in equilibrium with the melts from which they precipitated and the liquidus temperature of basaltic melts is proportional to the MgO contents in the melts[55–57]. Thus the Mg# and liquidus temperatures of the melts crystallizing cumulus minerals can be calculated using the well-established Fe-Mg exchange coefficients ($K_D(\text{Fe-Mg})^{\text{mineral-liquid}} = (Mg^{liquid}/Fe^{2+liquid})/(Mg^{mineral}/Fe^{2+mineral})$). Since meta-cumulates experienced HP granulite-facies metamorphism at the end of the Archaean and Fe-Mg re-exchanges should have occurred between minerals during this high-grade metamorphism, the compositions of pyroxenes or olivines present in the meta-cumulates cannot represent primitive compositions in equilibrium with the melts. However, the

595 K_D(Fe-Mg)$^{Cpx\text{-}liquid}$ (0.28 ± 0.08) is similar to the K_D(Fe-Mg)$^{Opx\text{-}liquid}$ (0.29 ± 0.06) and
596 the K_D(Fe-Mg)$^{Ol\text{-}liquid}$ (0.30 ± 0.03)[58,59], which allows us to use the bulk-rock Mg# of
597 the meta-cumulates to estimate the nature of their parental magma. Because of the
598 effect of trapped liquid crystallization on cumulus mineral compositions[60], the
599 calculated Mg# and liquidus temperatures should represent minimum estimates for the
600 equilibrated melts. The calculations are as following:
601 *Mg#(equilibrated melts) = 1/[(1/Mg#(bulk-rock) - 1)/Kd(Fe-Mg) + 1], where*
602 *Kd(Fe-Mg) = 0.28 for meta-websterites; 0.30 for meta-lherzolites;*
603 $T_{liquidus}$ *(°C) = 1,066 + 12.067Mg# + 312.3 (Mg#)*^{2}*;*
604 *Mg# = molar 100*Mg/(Mg + Fe).*

605 Data availability

606 The authors declare that all data supporting the findings of this study are available
607 within the main text, figures and Supplementary Information files.

608 References

609 43. Li X-H, Liu Y, Li Q-L, Guo C-H, Chamberlain KR. Precise determination of
610 Phanerozoic zircon Pb/Pb age by multicollector SIMS without external
611 standardization. *Geochemistry, Geophysics, Geosystems* 2009, **10**(4)**:** Q04010.
612 44. Sláma J, Košler J, Condon DJ, Crowley JL, Gerdes A, Hanchar JM*, et al.*
613 Plešovice zircon—a new natural reference material for U–Pb and Hf isotopic
614 microanalysis. *Chemical Geology* 2008, **249**(1-2)**:** 1-35.

615 45. Wiedenbeck M, Allé P, Corfu F, Griffin WL, Meier M, Oberli F*, et al.* Three
616 natural zircon standards for U-Th-Pb, Lu-Hf, trace element and REE analyses.
617 *Geostandards Newsletter* 1995, **19**(1)**:** 1-23.
618 46. Li X-H, Tang G, Gong B, Yang Y, Hou K, Hu Z*, et al.* Qinghu zircon: A working
619 reference for microbeam analysis of U-Pb age and Hf and O isotopes. *Chinese*
620 *Science Bulletin* 2013, **58**(36)**:** 4647-4654.
621 47. Stacey Jt, Kramers J. Approximation of terrestrial lead isotope evolution by a
622 two-stage model. *Earth and Planetary Science Letters* 1975, **26**(2)**:** 207-221.
623 48. Ludwig KR. *User's manual for Isoplot 3.0: A geochronological toolkit for*
624 *Microsoft Excel*. Berkeley Geochronology Centre, Special Publication, 2003.
625 49. Li X-H, Li W-X, Li Q-L, Wang X-C, Liu Y, Yang Y-H. Petrogenesis and tectonic
626 significance of the ~850 Ma Gangbian alkaline complex in South China:
627 Evidence from in situ zircon U–Pb dating, Hf–O isotopes and whole-rock
628 geochemistry. *Lithos* 2010, **114**(1-2)**:** 1-15.
629 50. Wiedenbeck M, Hanchar JM, Peck WH, Sylvester P, Valley J, Whitehouse M*, et al.*
630 Further characterisation of the 91500 zircon crystal. *Geostandards and*
631 *Geoanalytical Research* 2004, **28**(1)**:** 9-39.
632 51. Wu F-Y, Yang Y-H, Xie L-W, Yang J-H, Xu P. Hf isotopic compositions of the
633 standard zircons and baddeleyites used in U–Pb geochronology. *Chemical*
634 *Geology* 2006, **234**(1–2)**:** 105-126.
635 52. Morel MLA, Nebel O, Nebel-Jacobsen YJ, Miller JS, Vroon PZ. Hafnium isotope
636 characterization of the GJ-1 zircon reference material by solution and

637 laser-ablation MC-ICPMS. *Chemical Geology* 2008, **255**(1–2)**:** 231-235.
638 53. Pearce NJG, Perkins WT, Westgate JA, Gorton MP, Jackson SE, Neal CR*, et al.* A
639 Compilation of New and Published Major and Trace Element Data for NIST SRM
640 610 and NIST SRM 612 Glass Reference Materials. *Geostandards Newsletter*
641 1997, **21**(1)**:** 115-144.
642 54. Song SG, Su L, Li XH, Zhang GB, Niu YL, Zhang LF. Tracing the 850-Ma
643 continental flood basalts from a piece of subducted continental crust in the North
644 Qaidam UHPM belt, NW China. *Precambrian Research* 2010, **183**(4)**:** 805-816.
645 55. Weaver SJ, Langmuir CH. Calculation of phase equilibrium in mineral-melt
646 systems. *Computers & Geosciences* 1990, **16**(1)**:** 1-19.
647 56. Niu Y. Mantle melting and melt extraction processes beneath ocean ridges:
648 Evidence from abyssal peridotites. *Journal of Petrology* 1997, **38**(8)**:** 1047-1074.
649 57. Niu Y, Gilmore T, Mackie S, Greig A, Bach W. Mineral chemistry, whole-rock
650 compositions, and petrogenesis of Leg 176 gabbros: data and discussion.
651 Proceedings of the Ocean Drilling Program, Scientific Results; 2002: Ocean
652 Drilling Program College Station, TX; 2002. p. 1-60.
653 58. Roeder PL, Emslie RF. Olivine-liquid equilibrium. *Contributions to Mineralogy*
654 *and Petrology* 1970, **29**(4)**:** 275-289.
655 59. Putirka KD. Thermometers and barometers for volcanic systems. *Reviews in*
656 *Mineralogy and Geochemistry* 2008, **69**(1)**:** 61-120.
657 60. Barnes SJ. The effect of trapped liquid crystallization on cumulus mineral
658 compositions in layered intrusions. *Contributions to Mineralogy and Petrology*

1986, **93**(4)**:** 524-531.

Figure 1

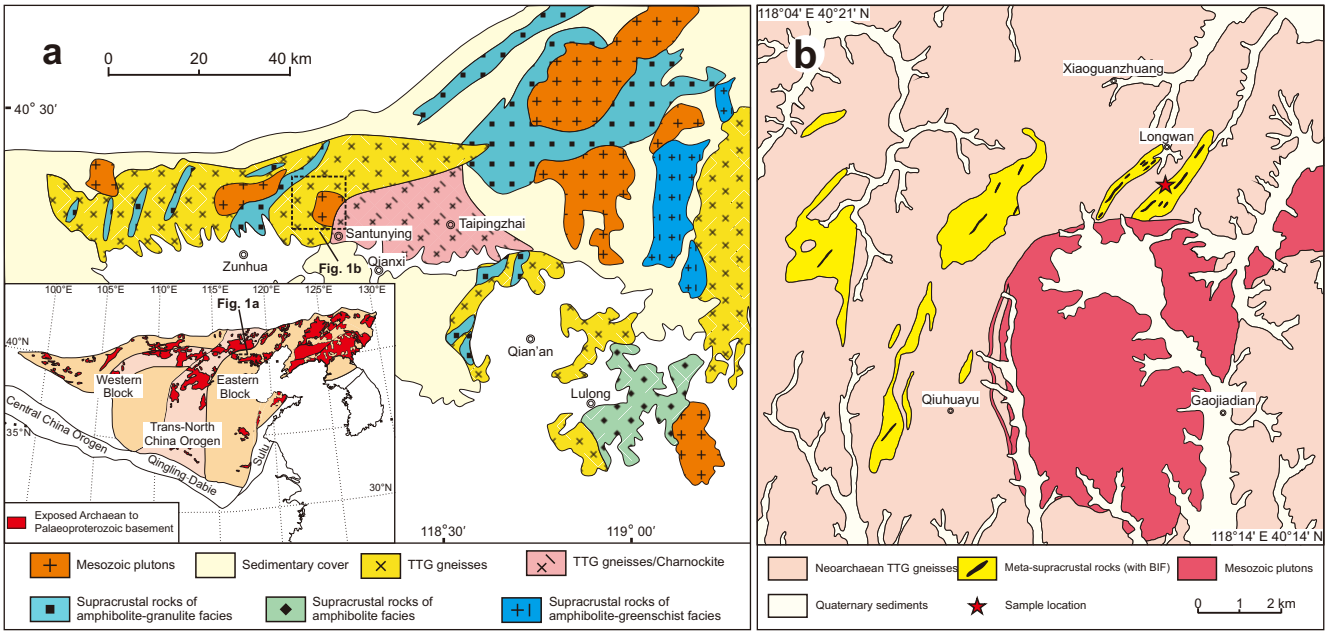
a
0
20
40 km
40° 30′
Zunhua
Santunying
Taipingzhai
Qianxi
Fig. 1b
Fig. 1a
Qian'an
Lulong
100°E
105°E
110°E
115°E
120°E
125°E
130°E
40°N
35°N
30°N
Western Block
Eastern Block
Trans-North China Orogen
Central China Orogen
Qinglin-Dabie
Sulu
Exposed Archaean to Palaeoproterozoic basement
118°30′
119° 00′
Mesozoic plutons
Sedimentary cover
TTG gneisses
TTG gneisses/Charnockite
Supracrustal rocks of amphibolite-granulite facies
Supracrustal rocks of amphibolite facies
Supracrustal rocks of amphibolite-greenschist facies
b
118°04' E 40°21' N
Xiaoguanzhuang
Longwan
Qiuhuayu
Gaojiadian
118°14' E 40°14' N
Neoarchaean TTG gneisses
Meta-supracrustal rocks (with BIF)
Mesozoic plutons
Quaternary sediments
Sample location
0
1
2 km

Figure 2

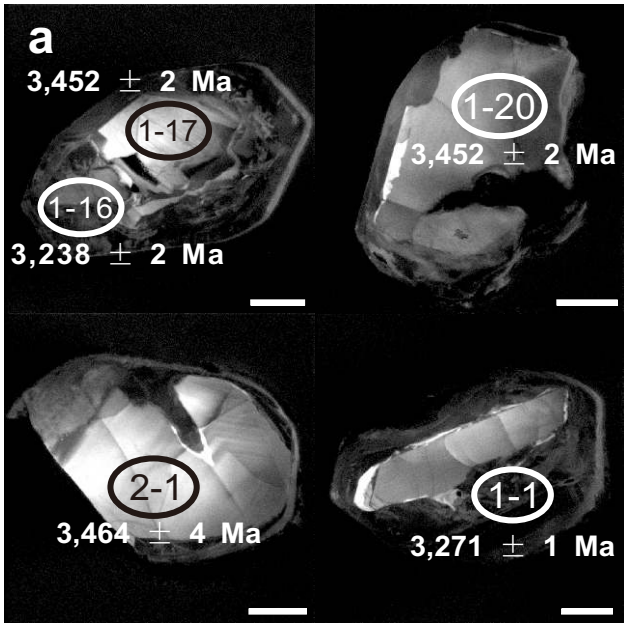
a
3,452 ± 2 Ma
1-17
1-16
3,238 ± 2 Ma
1-20
3,452 ± 2 Ma
2-1
3,464 ± 4 Ma
1-1
3,271 ± 1 Ma

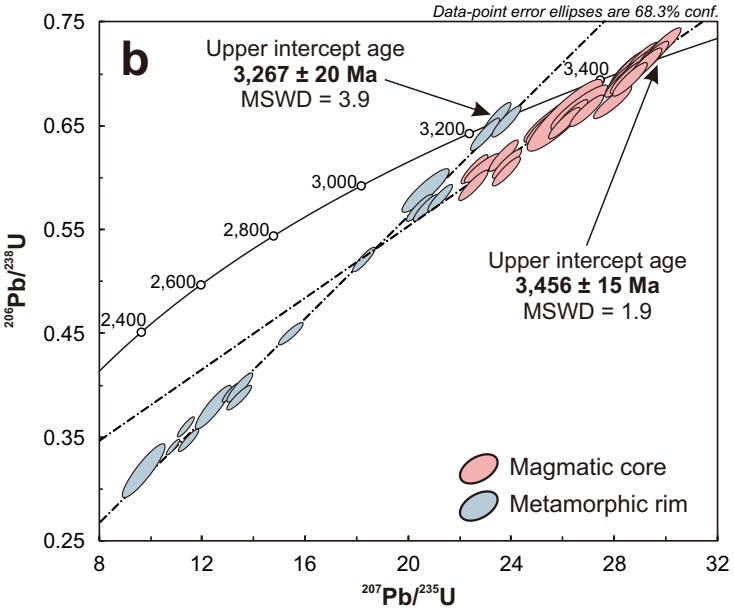
Data-point error ellipses are 68.3% conf.
b
Upper intercept age
3,267 ± 20 Ma
MSWD = 3.9
Upper intercept age
3,456 ± 15 Ma
MSWD = 1.9
Magmatic core
Metamorphic rim
206Pb/238U
207Pb/235U

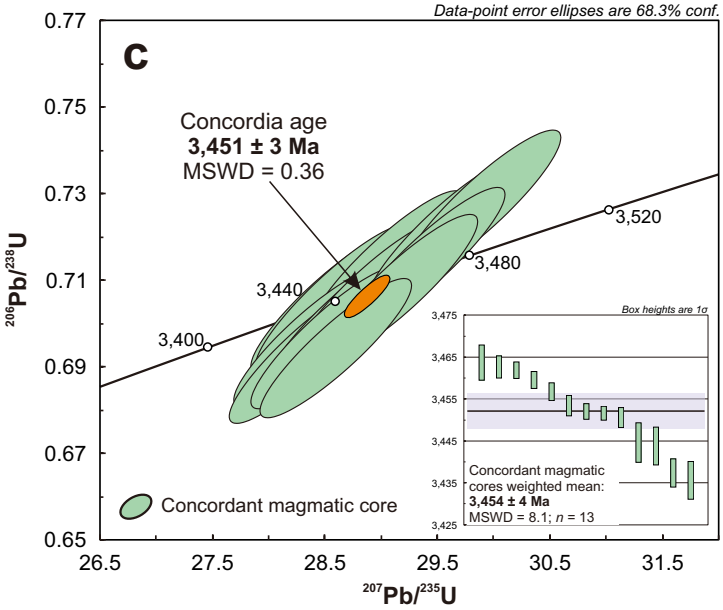
Data-point error ellipses are 68.3% conf.
c
Concordia age
3,451 ± 3 Ma
MSWD = 0.36
Concordant magmatic core
Box heights are 1σ
Concordant magmatic cores weighted mean:
3,454 ± 4 Ma
MSWD = 8.1; n = 13
206Pb/238U
207Pb/235U

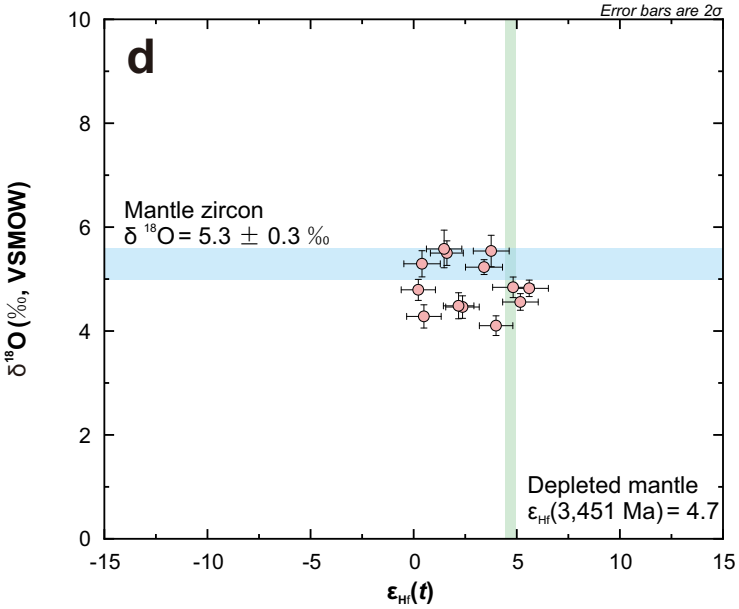
Error bars are 2σ
d
Mantle zircon
δ 18O = 5.3 ± 0.3 ‰
Depleted mantle
εHf(3,451 Ma) = 4.7
δ18O (‰, VSMOW)
εHf(t)

Figure 3

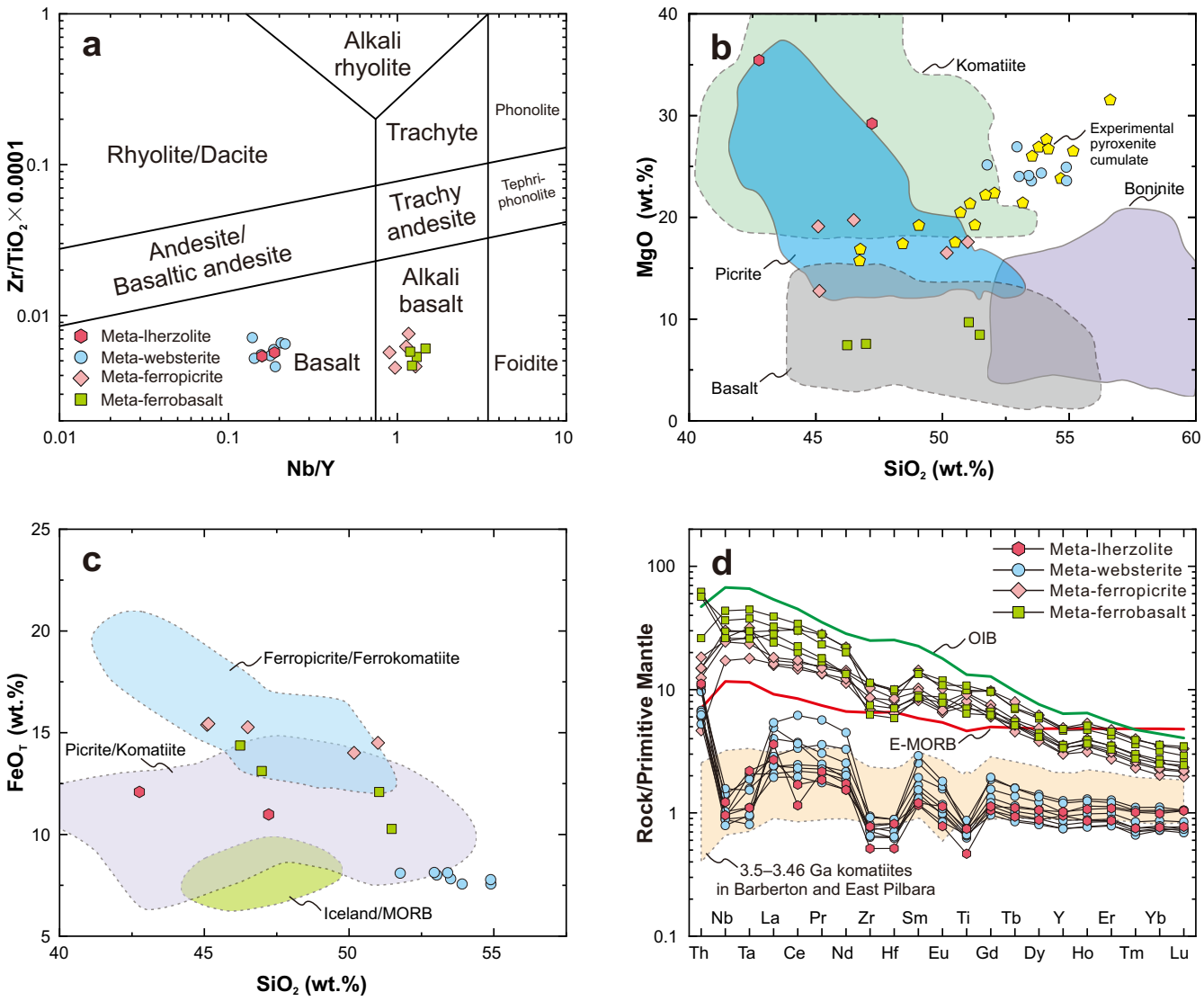
a
Alkali rhyolite
Rhyolite/Dacite
Trachyte
Phonolite
Trachy andesite
Tephri-phonolite
Andesite/ Basaltic andesite
Alkali basalt
Basalt
Foidite
Meta-lherzolite
Meta-websterite
Meta-ferropicrite
Meta-ferrobasalt
Zr/TiO2 × 0.0001
Nb/Y
b
Komatiite
Experimental pyroxenite cumulate
Boninite
Picrite
Basalt
MgO (wt.%)
SiO2 (wt.%)
c
Ferropicrite/Ferrokomatiite
Picrite/Komatiite
Iceland/MORB
FeOT (wt.%)
SiO2 (wt.%)
d
Meta-lherzolite
Meta-websterite
Meta-ferropicrite
Meta-ferrobasalt
OIB
E-MORB
3.5–3.46 Ga komatiites in Barberton and East Pilbara
Rock/Primitive Mantle
Th Ta Ce Nd Hf Eu Gd Dy Ho Tm Lu
Nb La Pr Zr Sm Ti Tb Y Er Yb

Figure 4

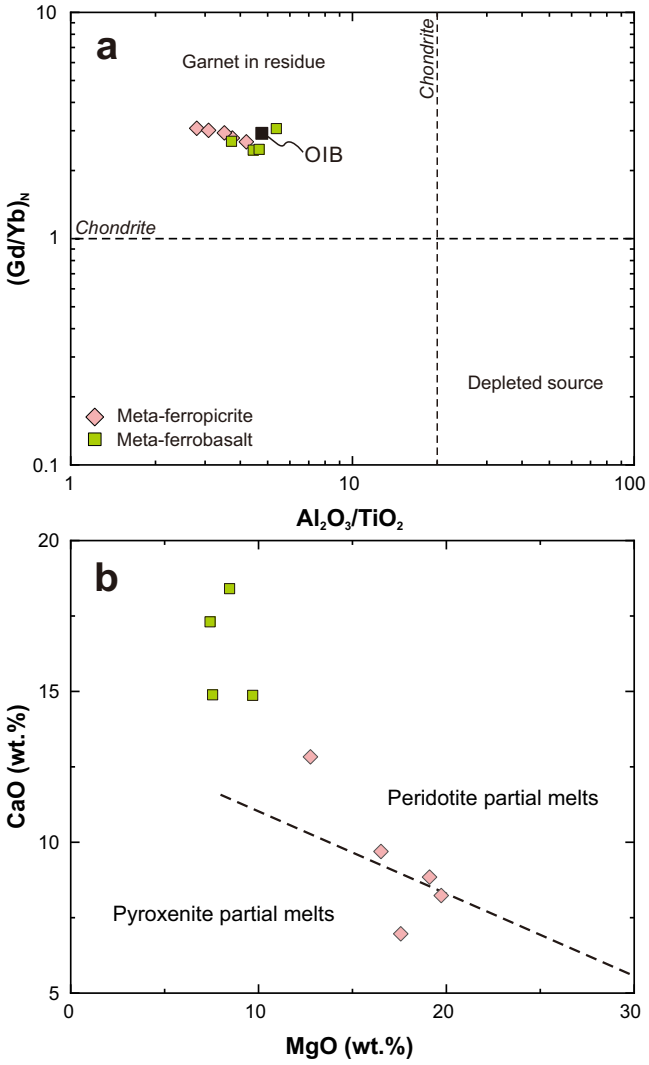
a
Garnet in residue
Chondrite
OIB
Chondrite
Depleted source
Meta-ferropicrite
Meta-ferrobasalt
10
1
0.1
1
10
100
(Gd/Yb)N
Al2O3/TiO2
b
Peridotite partial melts
Pyroxenite partial melts
20
15
10
5
0
10
20
30
CaO (wt.%)
MgO (wt.%)

Figure 5

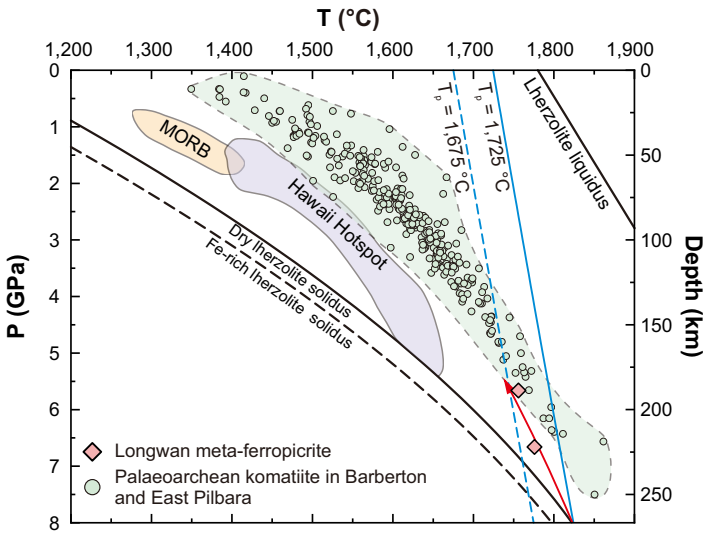
T (°C)
1,200
1,300
1,400
1,500
1,600
1,700
1,800
1,900
P (GPa)
0
1
2
3
4
5
6
7
8
Depth (km)
0
50
100
150
200
250
MORB
Hawaii Hotspot
Dry lherzolite solidus
Fe-rich lherzolite solidus
T$_p$ = 1,675 °C
T$_p$ = 1,725 °C
Lherzolite liquidus
Longwan meta-ferropicrite
Palaeoarchean komatiite in Barberton and East Pilbara